FINAL REPORT

Single Ferromagnetic Nanocontact Based Devices as Magnetic Field Sensors

SERDP Project MM-1593

MARCH 2008

Stanko R. Brankovic
Paul Ruchhoeft,
Sang –Eun Bae
Dustin Reynolds
Azeem Nasrullah
University of Houston

This document has been approved for public release.

Strategic Environmental Research and Development Program

This report was prepared under contract to the Department of Defense Strategic Environmental Research and Development Program (SERDP). The publication of this report does not indicate endorsement by the Department of Defense, nor should the contents be construed as reflecting the official policy or position of the Department of Defense. Reference herein to any specific commercial product, process, or service by trade name, trademark, manufacturer, or otherwise, does not necessarily constitute or imply its endorsement, recommendation, or favoring by the Department of Defense.

PROJECT : SEED MM 1593
FINAL REPORT: 03/10/2008

Single Ferromagnetic Nanocontact Based Devices as Magnetic Field Sensors

PI: Dr. Stanko R. Brankovic, University of Houston,
stanko.brankovic@mail.uh.edu

Co-PI: Dr. Paul Ruchhoeft, University of Houston

Other personnel: Dr. Sang –Eun Bae, Dustin Reynolds, and Azeem Nasrullah, University of Houston

PROJECT SUMMARY

The research program under designation SEED MM1593, funded by SERDP in a period of one year (03/01/2007 – 02/29/2008) has yielded positive results which can be briefly described as:

1. Successful development of ferromagnetic nanocontact material (metal-metal oxide/hydroxide) for magnetic nanocontact based magnetic field sensor fabrication,
2. Development and integration of electrodeposition, e-beam lithography and reactive ion etching processes necessary for fabrication of magnetic field sensor devices having the critical dimensions of ~30 - 40 nm (nanocontact diameter).
3. Fabrication and testing of 50+ prototype devices with an average value of magnetoresistance ~ 32%, measured at room temperature.
4. The immediate results produced during this research program have been published in two peer reviewed journal publications [1,2] and presented at 2007 SERDP workshop in Washington DC. An additional publication with an indirect relevance to this program has been published as a result of a broader collaboration with other researchers in the ECE department, University of Houston [3].

The novel device and ferromagnetic nanocontact material as well as the facile device fabrication concept have clearly demonstrated a cost effective route for transformative development of sensing devices for the underground munitions detection applications. The new sensing concept could have the great potential for further improvement of the US army detection systems.

PRIOR ART

In recent years, the phenomenon called "Ballistic Magnetoresistance" or "BMR" has been introduced to the scientific community [4,5,6,7,8,9,10]. The "BMR" phenomenon was associated with the existence of ferromagnetic nanocontacts, and the idea of "*nanocontact*" based devices has drawn considerable attention due to the potential application as magnetic field sensors and magnetic random access memory devices (MRAM) [11]. The accurate description of the "BMR" phenomenon is still a topic of scientific discussions and several models are offered in the literature [12,13,14,15,16,17]. The most receptive one is based on the spin dependent electron scattering from the magnetic domain wall (MDW) existing in the confined geometry of the nanocontact between two ferromagnetic electrodes [4,16,13] (Figure 1). If the size of the nanocontact containing MDW is the same or less than the spin flip mean free path of the electrons, *i.e.*, the electron transport through the MDW is ballistic ($d, w \sim \lambda_f$), then electrons passing through the MDW will encounter a high reflection probability due to the poor matching of the Fermi surfaces of spin-up and spin-down electrons. This manifests as a higher resistance state than when both electrodes have the parallel magnetizations pointing along the same direction (non-existing MDW).

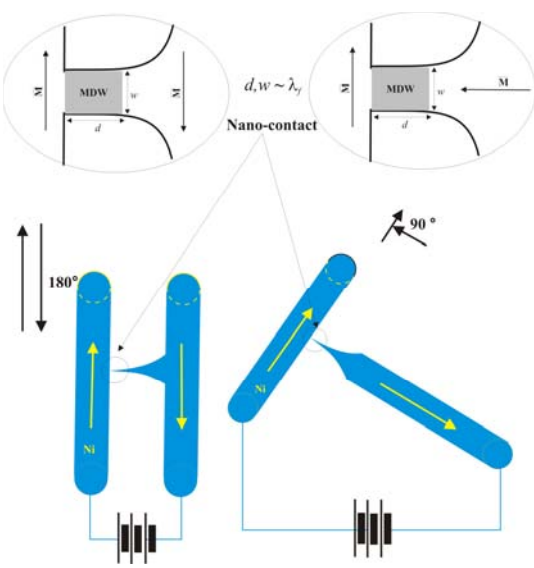

Figure 1 *Geometry of the electrodeposited nanocontacts between two ferromagnetic electrodes. Mutual orientations of the electrodes' magnetizations are 180º (left) and 90º (right). The insets show the schematics of the high resistance state related to nano-confinement of the MDW.*

The best results reporting "BMR" ($\Delta R/R_{min}$ = 300% - 3000%) involve nanocontacts created by electrodeposition [8,18]. However, Svedberg and co-workers pointed out [19] that, if experimental conditions are such that a dendritic electrodeposit is formed [20], the large values of magnetoresistance can be produced by the motion of the magnetic nanoparticles within the agglomerate forming the nanocontact. This effect could contribute to the large magnetoresistance observed in original experiments reporting the "BMR" phenomenon [4,5,6,7,8]. Egelhoff *et al.* have considered experimentally and theoretically the possibility that, in the case of Ni, Fe or Co electrodes, the magnetostriction can contribute to the observed large values of

magnetoresistance [14]. Nevertheless, Garcia *et al.* have offered recently the experimental evidence excluding the magnetostriction as the origin of the "BMR" [21].

One of the key issues related to ferromagnetic nanocontacts with large magnetoresistance is the possibility of oxide incorporation during nanocontact electrodeposition. The nature of the control in electrochemical cell [22] requires, that during Ni, Co, or Fe electrodeposition on the cathode side, the oxidation of the same metal serving as an anode has to occur simultaneously in order to have the continuity of charge flow through the cell [22]. The broad region of passivity for Ni, Co or Fe metals at more positive potentials [23] provides the situation where, in the moment of the nanocontact formation, the metallic cathode surface is connected with an anode covered by an oxide layer. Mallet *et al.* [24] have shown that, if there is no oxide on the anode surface before the nanocontact is formed, no significant magnetoresistance is observed. The importance of the oxide in nanocontact geometry has been also pointed out by Tsymbal *et al.* [15]. In this work, the authors showed that presence of an incoherent metal oxide layer, with disorder or impurities between two ferromagnetic nanoelectrodes, gives a rise to the phenomenon called "*resonant inversion of tunnelling magnetoresistance*". This phenomenon can explain the origin of the positive and negative magnetoresistance observed in some electrodeposited nanocontacts [25]. The tunnelling phenomenon occurring within the metal/oxide nanocontact junctions has been also elaborated by Garcia [16] emphasizing that the phenomenological distinction between tunnelling in ballistic nanojunctions and ballistic magnetoresistance cannot be achieved by experimental measurements.

DEVICE FABRICATION-Lithography and Etching Process Development

The approximate device geometry that has been pursued in our research is shown schematically in Figure 2A. The device concept is designed as plain parallel 90 ° mutual orientation bottom and top magnetic wires (leads) insulated by ~50 nm thick Al_2O_3 layer. The wires are connected by the ferromagnetic nanocontact formed by electrodeposition in the nanoconfined electrode geometry which represents the etched cylindrical hole in insulating Al_2O_3 with diameter of ~ 30 - 40 nm. Both wires and nanocontact are produced by electrodeposition, and the material of the bottom wire is either Ni, or Co, while the material of the top wire is Permalloy. The device build is implemented as bottom-up fabrication process and the most important results related to the development of each of these processes will be discussed latter in the text.

The top view of our prototype device is shown in Figure 2B (optical image) and the zoom of the region where the two magnetic wires overlap is

shown in Figure 2C. The each wire is indicated in the Figure 2B. The region of the device where the magnetic wires are connected by ferromagnetic nanocontact is shown with circle – dashed line, and the actual FIB-cross-section of the device showing the connection between the magnetic wires with ~ 45 nm diameter, Ni nanocontact is shown in Figure 2D.

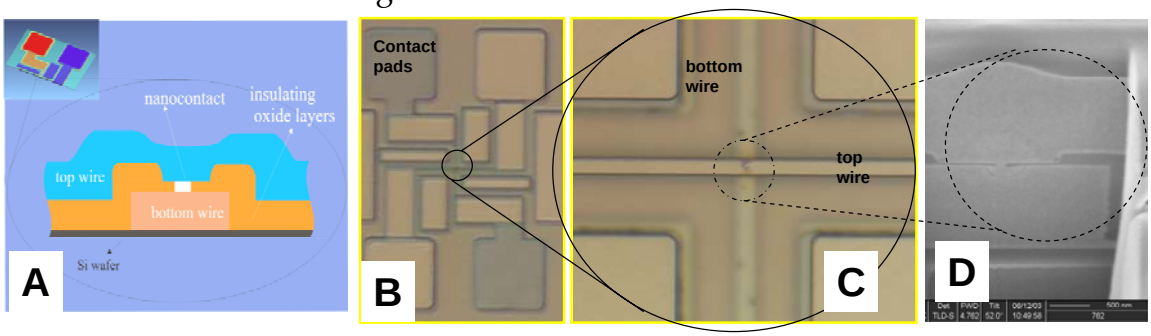

Figure 2. *A) schematics of the device design and cross-section showing bottom and top magnetic wires, nanocontact and insulating layer,(B) Top view optical image of the actual prototype device, (C) Zoom of the critical part of the device where the top and bottom wire connect with nanocontact (top view) and (D) FIB-SEM of the cross-section of the actual device having ~45 nm diameter of the nanocontact (material: Ni/Fe(OH)$_3$).*

E-beam lithography Results. The device design and corresponding fabrication process relied on the lithography to deliver the defined nanohole dimensions of the mask for etching of the nanoholes and for electrodeposition of ferromagnetic nanocontacts. The initial trials to use ion-beam lithography as a high throughput and low cost approach were abandoned in the period May-Jun 2007 due to the difficulties in making stencil masks with appropriate nano-aperture dimensions. For this reason, all our efforts were invested in the e-beam lithography as the main tool to create the desired nanoelectrodes geometry. In this work, we used approach developed earlier by PI where the 100 – 200 nm thick PMMA resist is used with 10 nm thick underlayer of PMGI [26].

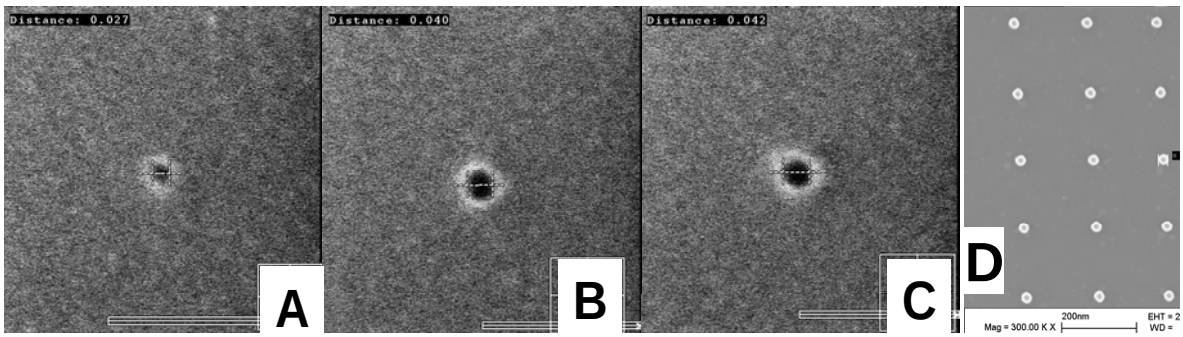

Figure 3. *E-beam lithography results (A) ~27 nm (B) ~40 nm and (C) 42 nm nanoholes produced in 100 nm PMMA resist using does of 70, 140 and 250 μC. (D) Array of ~40 nm diameter Ni nanodots electrodeposited into a nanohole electrode array produced by e-beam lithography.*

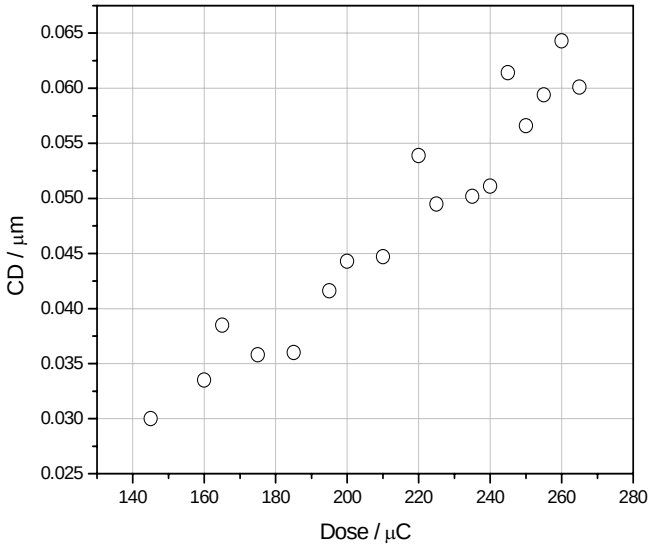

Figure 4. *Dose matrix for e-beam process. System: 100 nm PMMA/50nmAl2O3/100 nm of Co. The actual dimensions of the measured diameter of the nano-holes pattern vs. does used in single e-beam pass.*

The best results that were achieved for single nano-hole geometry were in the range of 30 nm, however, the typical yield in this dimension range was low, ~30% (Figure 3). The optimum e-beam lithography was developed for the nano-holes with ~ 40 nm diameters (yield ~90%) where the subsequent electrodeposition of Ni has been used to verify the success of the of the process and cleanness of the nanoholes after developer is applied to remove the exposed resist. The typical lithography and subsequent Ni electrodeposition results are shown in Figure 3 and the dose matrix developed for e-beam process for 50 nm CAD dimensions of the nanohole is shown in Figure 4.

Reactive Ion Etching.

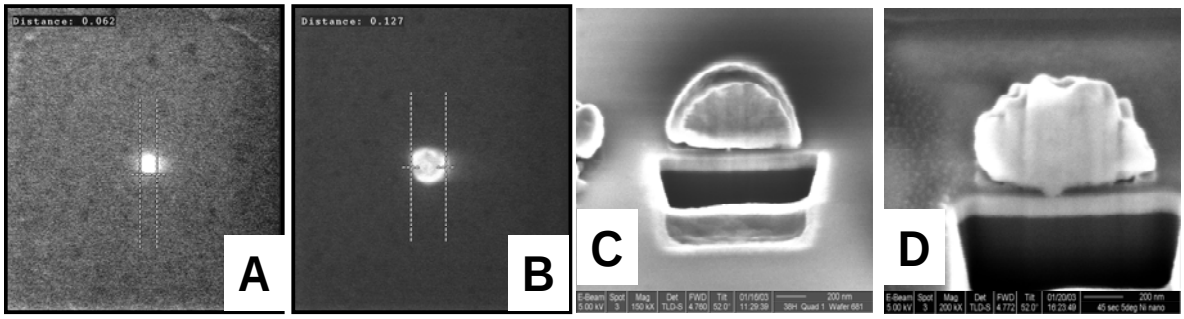

Figure 5. *RIE results from nanohole electrode geometry. The test structures are etched in 50 nm Al_2O_3/100 nm Co, having 100nm of PMMA with e-beam defined nanohole mask pattern. (A) and (B) are ~60 nm and 120 nm diameter of etched holes in Al_2O_3 layer measured immediately after etching step. (C) and (D) are FIB cross-section of the electrodeposited Ni into a 30 nm and 45 nm nanohole electrode geometry. The large mushroom like Ni overgrowth on top of the metal deposit in nanocontact electrode geometry is formed purposely to facilitate the identification of the location of deposited and etched structures.*

The RIE etching process using CHF_3 gas was developed for fabrication of nanohole electrode geometry in insulating Al_2O_3 layer. The natural stopping material for etching process was metal layer (Co, or Ni) as a part of underlying magnetic leads. The success of the etching process during the process development stage was also verified by subsequent Ni electrodeposition and the typical yield was found to be ~80 %. The great difficulty was experienced in measuring the real size of the etched holes immediately after etching. This problem was related to strong charging of the samples in high resolution SEM image mode resulting in inaccurate evaluation of dimensions (50% larger than real dimensions). Because of this, the SEM of the fibbed Ni electrodeposits in nanohole electrode geometry was used to verify and compare the nanohole dimensions with the ones expected from the e-beam lithography metrology. It was concluded on more than a dozen comparative measurements that the size of the etched holes is typically ~5-10% larger than the one defined by e-beam lithography. The representative results and metrology from this step are shown in Figure 5.

ELECTRODEPOSITION OF NANOCONTACTS

Ni Nanocontact with phase separated Ni and oxide/hydroxide domains ($Fe(OH)_3$). Our approach to form the Ni nanocontacts with certain amount of oxide/hydroxide phase was based on the following phenomenon. During electrodeposition of the ferromagnetic metals and alloys, the hydrogen co-deposition occurs in parallel leading to the depletion of the hydrogen ions at the electrode/solution interface. This causes the local increase in *pH* which promotes the nucleation and precipitation of insoluble *M(OH)n* species at the growing electrode/solution interface. This process is attributed as the main reason for incorporation of oxide and nonmagnetic inclusions in *Permalloy* [27], *CoFeNi* [28] and in 2.4 [T] *CoFe* alloys [29]. Our research work in the first six months has been focused on phenomenological description of this process and experimental measurements demonstrating that the incorporated hydroxide exists as completely separate phase in magnetic deposit [1]. The hydroxide incorporation rate is equal to the hydroxide flux achieved through the nucleation/precipitation process ($mol \cdot cm^{-2} \cdot s^{-1}$) and it is defined as function of metal ions forming the insoluble $M(OH)_n$ hydroxide as [1]:

$$R_{hyd} = N \cdot \Xi \cdot \exp\left(-\frac{16\pi \cdot \sigma_{hyd}^{3} \Omega^{2}}{3k^{3}T^{3} \cdot \left(\ln\left(\frac{C_{\infty,M^{n+}}}{\frac{K_p}{(K_w)^n} \cdot \left(10^{-pH} - \frac{(1-\gamma)\cdot j}{F} \cdot \frac{\delta}{D_{H^+}} \right)^n} \right) \right)^2} \cdot \phi \right) \qquad (1)$$

In the above expression, the ϕ is the shape factor of the nucleus while $N \cdot \Xi$ represents the product between the average size of hydroxide stable nucleus and nucleation rate constant. These are the only parameters that have to be determined experimentally, while the values of pH, δ, j, and γ represent the pH of the solution, diffusion layer thickness, current density and current efficiency and they are the parameters related to the solution and electrodeposition process design. The other terms in eq.(2) are physical constants which are available in literature or they could be calculated from the published data (n is oxidation state of the metal ions forming insoluble hydroxide, Kp is product of solubility of the metal hydroxide, Kw is the ionic product of water, F is Faraday's constant, D_{H+} is diffusivity of hydrogen ions, T is absolute temperature, σ_{hyd} is the surface energy of hydroxide, Ω is the molecular volume of hydroxide).

We use the above expression to find the volume fraction of the hydroxide phase in magnetic deposit by simple formula [1]:

$$vol_{hyd} = \frac{R_{hyd} \cdot \upsilon_{m,hyd}}{R_{FM} \cdot \upsilon_{m,FM} + R_{hyd} \cdot \upsilon_{m,hyd}}, \qquad (2)$$

where R_{FM} represents the deposition flux of ferromagnetic phase which is calculated from the deposition current j, and current efficiency γ as $R_{FM} = j \cdot \gamma / nF$, while $\upsilon_{m,hyd}$ and $\upsilon_{m,FM}$ are the molar volumes of metal-hydroxide and ferromagnetic phase which can be evaluated from the literature.

The most insoluble hydroxide among the ferromagnetic metals is $Fe(OH)_3$, and the easiest approach to incorporate the oxide phase into the Ni as the ferromagnetic phase, or any other ferromagnetic metal is to add certain amount of Fe^{3+} into solution for Ni deposition. In order to determine the shape factor ϕ and product $N \cdot \Xi$ in eq.(2) for incorporation process of $Fe(OH)_3$ we have measured the magnetic moment of electrodeposited $Co_{40}Fe_{60}$ films as a function of the vol. fraction of the incorporated hydroxide phase.

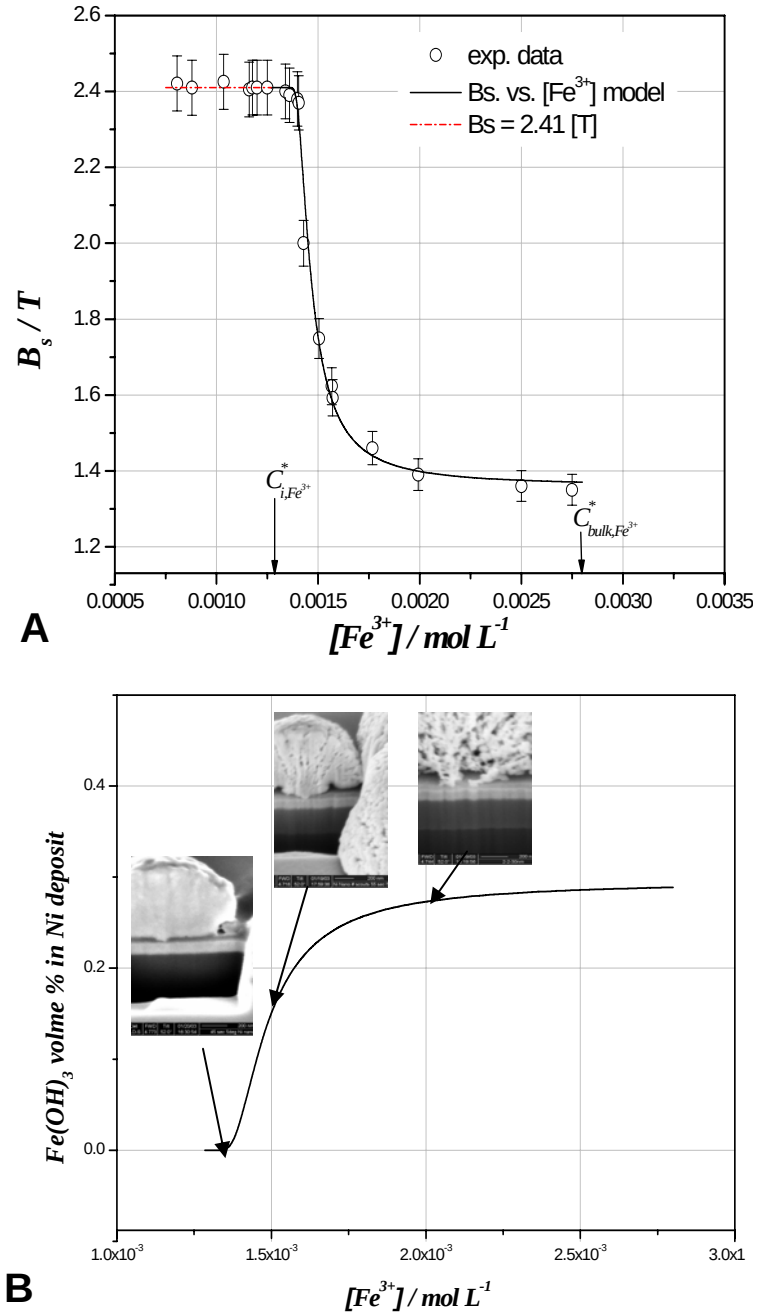

Figure 6. (A) *Bs vs. [Fe^{3+}] for electrodeposited $Co_{40}Fe_{60}$ films. The concentrations of Fe^{3+} for which the onset of $Fe(OH)_3$ nucleation starts at interface (*) and in the bulk solution (∞) are indicted in the graph. Solution: pH=2, [Fe^{2+}] = 0.1 M, [Co^{2+}]=0.05 M, H_3BO_3 = 0.4 M, NH_4Cl = 0.3 M, Deposition parameters: j=3.8 mAcm^{-2}, γ=0.12, ω= 300 rpm [1].*
(B) *Calculated vol_{hyd} vs. [Fe^{3+}] dependence for electrodeposited Ni films using ϕ = 8.2 $\times 10^{-6}$ and $N \cdot \Xi$=2.35 $\times 10^{14}$ cm$^{-2}\cdot$s^{-1} determined from the model fit to the data in Figure 6A. Solution for Ni deposition: pH=2, [Ni^{2+}] = 0.1 M, H_3BO_3 = 0.4 M, Deposition parameters: j=4 mA·cm^{-2}, γ=0.25, ω = 300 rpm. The insets in Figure 6B are SEM images of the FIBs of Ni nanodeposit obtained from the solutions having 1.35x10^{-3} mol·L^{-1}, 1.5x10^{-3} mol·L^{-1} and 2.5x10^{-3} mol·L^{-1} of Fe^{3+}.*

The example of this procedure is shown in Figure 6, for deposition of $Co_{40}Fe_{60}$ films. The magnetic moment of CoFe is fitted by following expression [30];

$$Bs = Bso \cdot (1 - vol_{hyd}) \quad (3)$$

where Bso =2.41 T is the magnetic moment of pure CoFe phase. The vol. fraction of hydroxide phase vol_{hyd} is expressed as a function of Fe^{3+} concentration in the solution using the eq.(1) and eq.(2). The fit of the eq.(1-3) to the Bs vs. [Fe^{3+}] data in Figure 6A, yields the values of parameters ϕ and $N \cdot \Xi$ necessary for complete phenomenological description of the $Fe(OH)_3$ incorporation process. We used these parameters to predict the volume fraction of $Fe(OH)_3$ in electrodeposited Ni as a function of Fe^{3+} concentration in Ni plating solution. This calculation is shown in Figure 6B. The insets in this figure represent the FIB cross-sections of Ni nanocontact deposit with different vol% of $Fe(OH)_3$ phase.

The EDX analysis of the Ni deposit for O content was fond in good agreement with our vol% of $Fe(OH)_3$ phase estimate in Ni matrix. Also, the SEM images of the corresponding Ni deposit with different amount of incorporated $Fe(OH)_3$ do show a significantly different contrasts. The samples with *vol%* above 10% do show pronounced dark regions which according to NANOEDX measurement are iron and oxygen reach phase-particles, or $Fe(OH)_3$ phase. The described procedure, deposition process, and solution formulation for Ni nanocontact deposition with controlled amount of oxide/hydroxide phase is used for fabrication of the magnetic field sensors with nanocontact with phase separated ferromagnetic Ni matrix and hydroxide ($Fe(OH)_3$) domains.

Ni Nanocontacts with Ni_xO_y Layer Formed by Anodic Oxidation. The second approach to fabricate Ni nanocontacts with controlled amount of oxide phase is based on the application of one short anodic pulse during the nanocontact electrodeposition. The typical current transient from Ni nanocontact electrodeposition/oxidation is shown in Figure 7A. The deposition process involves three steps, 1) electrodeposition 2) anodic oxidation and 3) electrodeposition again in order to form Ni/Ni-oxide/Ni structure with in the boundary of the nanoelectrode confinement. The electrodeposition and anodic oxidation of Ni is performed in the same solution. The anodic pulse towards the potential region of Ni passivity yields the irreversible formation of Ni-oxide layer that can not be reduced upon the potential reversal back to the deposition regime [31]. The anodic formation of Ni-oxide has been well understood within the realm of *Point Defect Model* and experimental data were found in a good agreement with predictions of the theory [32].

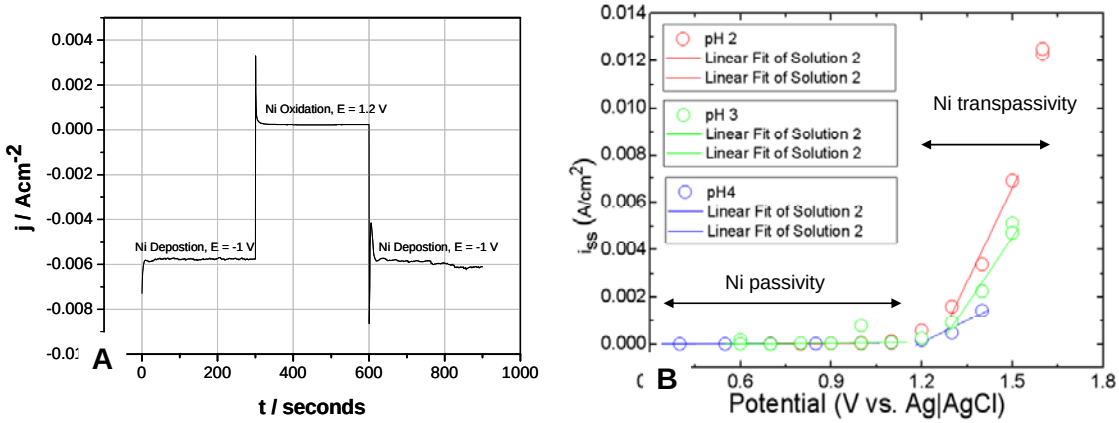

Figure 7 *(A) Typical current transient from Ni Electrodeposition/oxidation/electrodeposition process. Solution: 0.1 M* Ni^{2+} *+ 0.4 M* H_3BO_3*, pH = 2. (B) Steady state current transients for anodic oxidation of Ni surface obtained for different anodic potentials and pH. The two different slopes of* i_{ss} *vs. E indicate the two potential regions of Ni passivity and transpassivity.*

There are two types of Ni-oxide that are explored in our fabrication concept. The first one is the compact but defective inner *NiO* barrier layer (1-3 nm) which is formed in the passive potential region. There is considerable evidence that *NiO* layer is highly ordered with epitaxial crystalline structure on metal substrate [33]. This layer is covered with >2 nm $Ni(OH)_2$ outer phase [34] which can not be reduced upon reversal of the potential back to deposition regime. The second type of Ni-oxide is formed by anodic potential pulse in trans-passive potential region. This oxide is not stoichiometric, it has low density and its reduction to *NiO* or $Ni(OH)_2$ was found during the reversal of the potential into cathodic/deposition region [35]. The anodic potentials yielding the formation of these two types of Ni-oxide layers is determined by analysing the steady

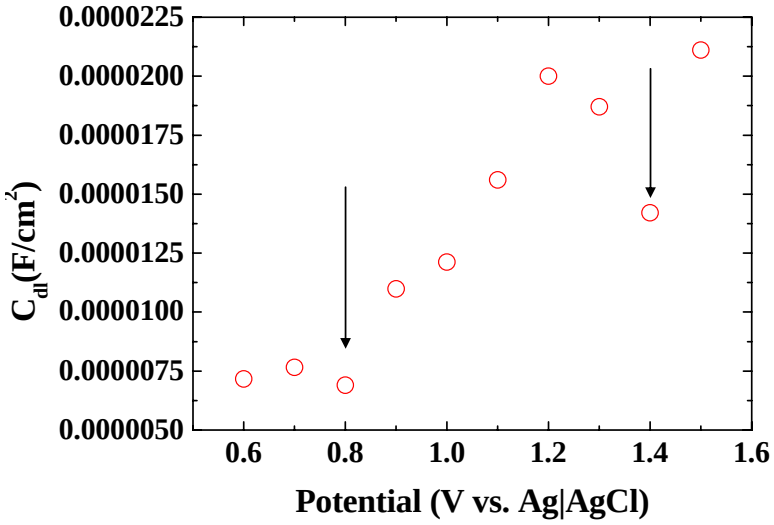

Figure 8. *Double layer capacitance for anodized Ni electrode at different potentials for 300 sec in 0.1 M* Ni^{2+} *+ 0.4 M* H_3BO_3*, pH = 2. Arrows indicate minima for passive and traspasive potential regions.*

state current transients from our anodic pulse potential experiments [32]. These results are shown in Figure 7B for solution design: 0.1 M Ni^{2+}, 0.4 M H_3BO_3 and pH ranging from 2 to 4. The choice of particular anodic pulse potential to form Ni-oxide layers in passive and trans-passive region is based on the measured values of the double layer capacitance of the oxidized Ni electrode by 300 second long anodic pulse. The chosen potentials of +0.8 V and 1.4 V vs. Ag+/AgCl/Cl^- electrode are the ones where the minimum double layer capacitance is measured for each potential region which indicates formation of the particular oxide layer with the minimum thickness [36], Figure 8. The duration of the anodic pulse during the Ni nanocontact fabrication for each potential is determined as the time necessary for establishment of the steady state anodic current, *i.e* the formation of the oxide layer with uniform thickness [32]. For both anodic potential pulses Δt is determined to be ~ 50 seconds.

Ni Single Crystal Nanocontacts. The magnetic field sensors with single crystal Ni nanocontacts represent structures where the electron transport occurs with minimal scattering from crystal defects such as grain boundaries, dislocations, inclusions etc**.** They are used as referent point to which the performance and properties of devices with different amount of oxide/hydroxide within the nanocontact matrix can be compared to, and the relative contribution of oxide/hydroxide content to the values of the resistance is evaluated (ΔR/R vs. vol% oxide).

The methodology for design of successful and precise electrodeposition process of Ni single crystal in the nanotemplate electrode geometry is based on earlier PI's work on CoFe and CoNiFe deposition at nanoscale in a trench electrode geometry ($d \leq 50$ nm) [37 , 38]. In this work, the successful electrodeposition process has been developed by fully considering the transport limitations in nanoconfined electrode geometry [37,38], conditions at the electrochemical interface for additive adsorption [39], and interface stability with respect to $Fe(OH)_3$ precipitation [38]. The additional effect that we have exploited for nano-hole electrode geometry is that it serves as an effective promoter of a perfect mononuclear layer-by-layer growth. The theoretical base for this effect has been offered in the literature considering the kinetics of thin film growth [40,41,42,43]. According to this considerations, the nucleation density, *n,* is a function of deposition flux ($F=j\gamma/nF$), the nearest neighbor distance for an atom diffusion over the surface (a), and the surface diffusivity (D), as;

$$n \approx \left(\frac{F}{a^2 \cdot 4D} \right)^{1/3} = \left(\frac{j \cdot \gamma}{nF \cdot a^2 4D} \right)^{1/3}$$

By taking an a~0.3 nm (Ni), D~ 10^{-6} cm^2s^{-1} [44], $\gamma = 0.2$, and nF ~2×10^5 $C \cdot mol^{-1}$, we have estimated the current density that should produce the single Ni nucleus per

nano-electrode area. The square root of the $1/n$ is taken to be equal to the nano-hole electrode geometry with diameter d~40 nm, and the deposition current density (flux) leading to the mononuclear layer by layer growth is found to be ~ < 0.01 mA/cm^2. The example of single crystal Ni overgrowths originating from a single nanoelectrode geometries are shown in Figure 8A and 8B. The diameter of the nanohole electrode is d ~ 40 nm and the cuboctahedral shape of the Ni overgrowth deposit obtained after bottom-up deposition (j ~ 0.006 mAcm^{-2}) indicates single crystal structure. The representative FIB cross-section of the nanocontact defined in Al_2O_3 layer is shown in Figure 8C. The facets defining the Ni deposit shape represent the FCC metal low-index planes developed during the deposit growth. The cuboctahedral shape of the deposit in the half space above the insulating layer is defined by the minimum of the single crystal's surface free energy [45] which indicates that the Ni nanocontact from which this electrodeposit evolves is single crystal as well.

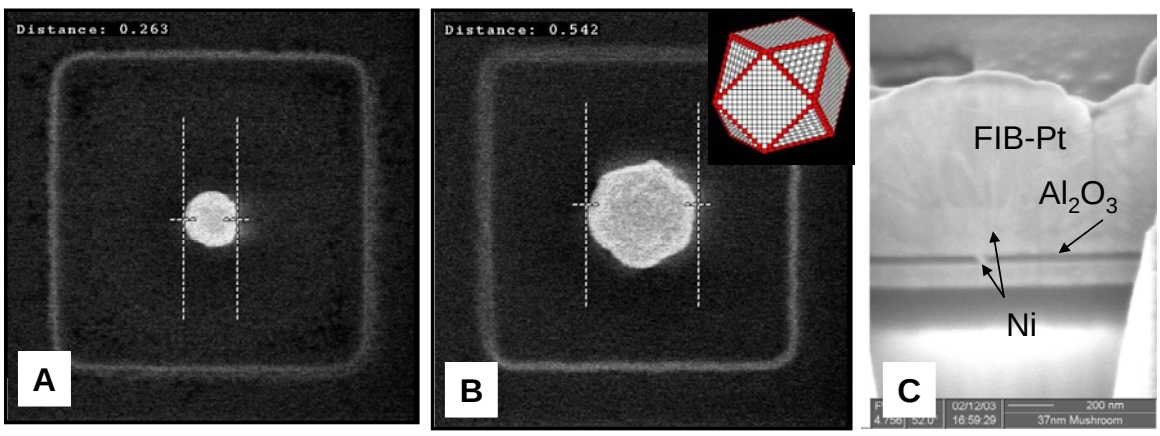

Figure 8. *(A) and (B) Top view of Ni clusters electrodeposited on top of the Ni nanocontact using current density of 0.006 mAcm^{-2}, inset shows the model of cuboctahedra (C) FIB cross-section of Ni 40 x 40 nm nanocontact corresponding to the structure in (B).*

DEVICE TESTING

The magnetoresistance measurements of devices are performed at room temperature as four probe resistivity measurements. The magnetic field was applied in the plane which is perpendicular to the current flow through the nanocontact as the crucial part of the device. The sweep limits of the magnetic field are designed to achieve full magnetization saturation in the ferromagnetic wires of the devices. The typical testing currents were 5 mA and 10 mA which assuming 40 nm diameter of the nanocontact correspond to ~ 4×10^{11} mAcm^{-2} and ~ 8×10^{11} mAcm^{-2} current density.

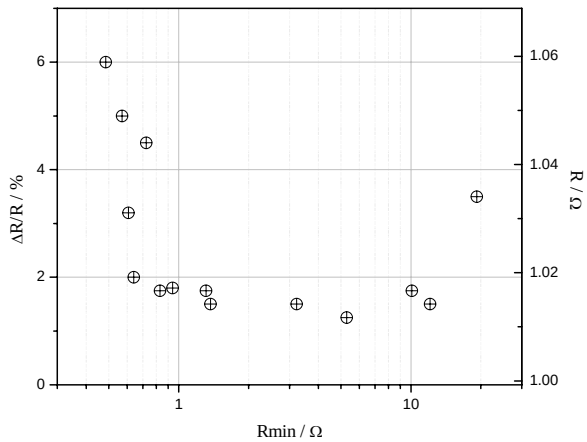

Figure 9. *ΔR/R vs. R_{min} for devices having Ni single crystal as the material of nanocontact and Ni (bottom) and Permalloy (top) as magnetic leads. Testing current is 5 mAcm^{-2}*

Prototype Devices with Ni single crystal nanocontact. The testing of the nanocontact devices with single crystal Ni nanocontact has not yielded any significant values of ΔR/R (Figure 9). For the achieved dimensions of the Ni nanocontacts being in average ~40 nm (lithography CD) and for the material of the magnetic wires being Ni (bottom) and NiFe (top) the measured values of the magnetoresistance were all in the range of 1- 3%, Figure 9. The values of R_{min} were found between 0.5- 10 Ω which might indicate a significant scattering in the real size of the nanocontacts cross-sections (conductive cross-section). Several devices have shown the ΔR/R values between 3-6% having R_{min} below 1 Ω which might be the indication that current crowding has contributed to the increased values of magnetoreistance. All observed values of ΔR/R can be understood within the frame of the anisotropic magnetoresistance (AMR) phenomenon and we conclude that no interesting information were obtained from this set of devices. Perhaps, either smaller CDs of the Ni nanocontact have to be achieved or the Ni + oxide material as nanocontact material is necessary in order to achieve the values of magnetoresistance comparable to the ones reported for BMR phenomenon.

Prototype Devices having Ni Nanocontacts with Ni_xO_y Layer Formed by Anodic Oxidation. The set of 12 devices that were built with this type of the nanocontact material did not yield any results. No connectivity between the bottom (Co) and top (Permalloy) magnetic leads was observed and no magnetoresistance measurements could be performed. The reason for this is not clear, however, the first FIBs of the failed devices indicate a disintegration of the nanocontact structure. This could happen during the device testing (high current, heating, etc) or during the fabrication of the devices (nanocontact dissolution during anodic pulse), Figure 10. At this point we are investigating possible reason for this failure. The additional efforts were made to produce a new set of devices with Ni/NixOy/Ni, structure, however, by the time this report is compiled, their fabrication and testing of these devices have not been accomplished yet.

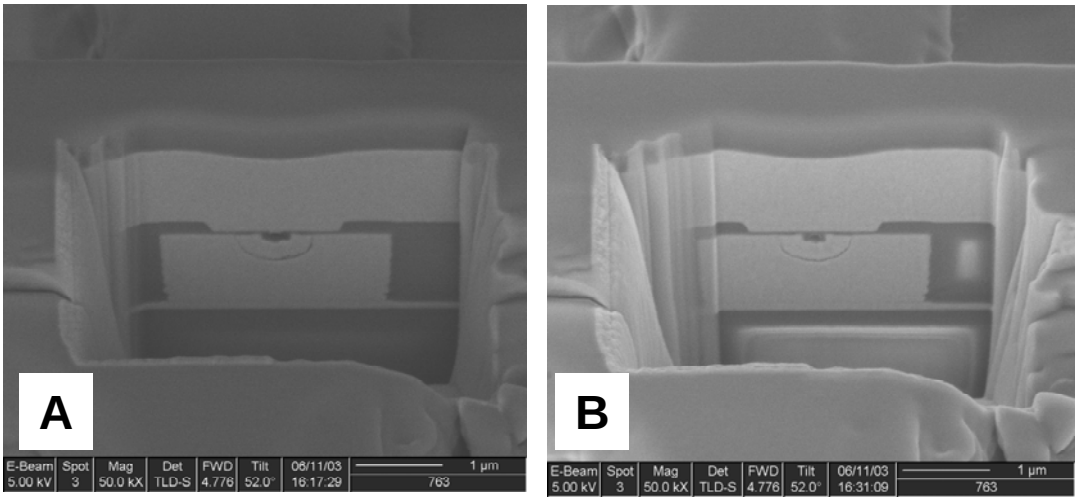

Figure 10. *(A) and (B) SEM of the FIB cross-sections of the prototype devices with Ni/NixOy/Ni nanocontact structure. On both images it is obvious lack of nanocontact between the two magnetic leads.*

Prototype Devices having Ni Nanocontact with phase separated Ni and oxide/hydroxide domains ($Fe(OH)_3$). This type of the devices produced the highest values of magnetoresistance, and for that reason, the most interesting results so far. The nanocontacts were produced by electrodeposition of Ni from solution: 0.1 M Ni^{2+} +0.4 M H_3BO_3 + 2 $\times 10^{-3}$ M Fe^{3+}, pH=2, which according to our model and experimental data (Figure 6B) produces Ni deposit with ~30% vol. of $Fe(OH)_3$ phase (j = 4 $mAcm^{-2}$). For these devices design, the bottom lead was made of Co, and the top one is made of Permalloy. During the testing the magnetic field was in plain perpendicular to the current of flow through the nanocontact and it was aligned along the direction of the Co –bottom wire, so that the switching of the magnetization is achieved only in the top lead (Permalloy). The ~30 % vol of the hydroxide phase ensures that Ni ferromagnetic phase percolates through the nanocontact body and therefore it should be expected to be responsible for the bulk values of the nanocontact resistance measured. The magnetoresistance values were measured for 50+ devices with an average nanocontact diameter of 40 nm (lithography). These data are shown in Figure 11A. As one can see, the R_{min} values were measured in between the 0.5 and 10 Ω. These values are similar to the ones obtained for devices with single crystal Ni nanocontact which additionally supports the fact that the current transport is entirely confined with in the Ni phase, and that tunneling phenomenon, or resonant tunneling, in this case can be excluded as the transport mechanism. The important fact from this data is that the $\Delta R/R$ vs. R_{min} dependence follows the universal scaling that is predicted theoretically by Garcia

et al [5] based on magnetoresistance originating from the electron scattering of the magnetic domain wall as the main mechanism for ballistic magnetoresistance. In our case, our exponent is -1, as shown by the ~32/R_{min} function fit of our data. Also it could be concluded that the average magnetoresistance for all devices is around 32%, the value that is comparable to the best GMR and TGMR based magnetic field sensors.

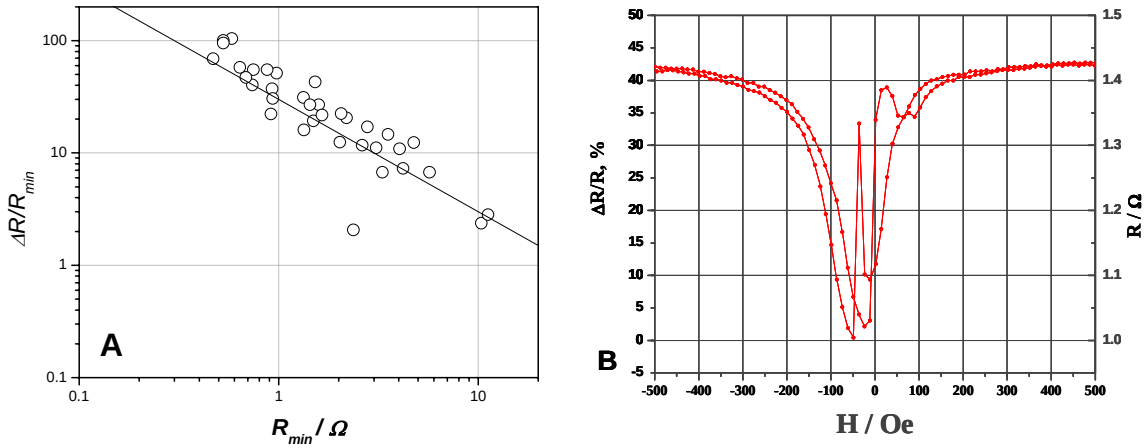

Figure 11 (A) *ΔR/R values measured for prototype devices having Ni nanocontact with phase separated Ni and oxide/hydroxide domains ($Fe(OH)_3$). The line represents the linear fit. (B) Representative magnetoresistance curve with R(H=0)>R(H=500 Oe).*

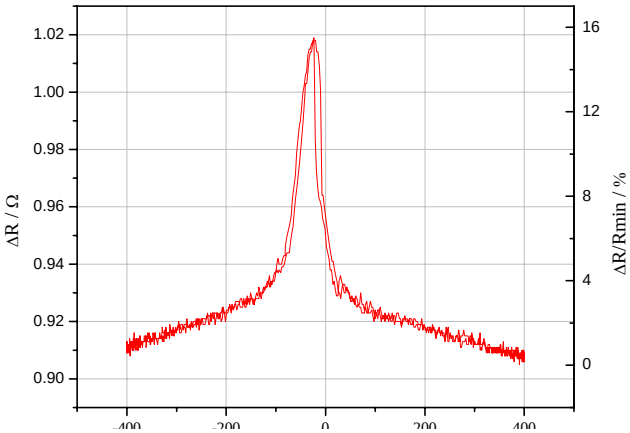

Figure 12. *ΔR/R and ΔR vs. H for devices having Ni-Ni oxide nanocontact structure. The material of wires is Co (bottom) and Permalloy (top). Testing current is 5 mAcm^{-2}*

In Figure 11B, the representative transport curve for the nanocontact with R_{min} = 1 Ω is shown. The ΔR/R measured is ~ 40%. As one can see, there are apparent hysterisis in the transport curve. This feature is reported earlier for ΔR/R curves involving resonant tunneling as the main transport mechanism in nanocontacts [15] and in our case it is still unclear what causes it. The presence of oxide phase in the nanocontact body certainly contributes to higher values of ΔR/R as compared to Ni single crystal nanocontacts devices (Figure 10), however, the similar values of R_{min} for both device

concepts exclude the tunneling and resonant tunneling as the main transport mechanism. More work is necessary to elucidate this intriguing result. In our measurements of the magnetoresistance for individual devices we do see the positive (R(H=0)>R(H=500 Oe)) and negative (R(H=0)<R(H=500 Oe)) values of ΔR/R. For comparison purpose we show transport curves in Figure 11B and Figure 12 as the two representative cases. It is important to say that same observation is reported by other researchers for BMR phenomenon [4,5,8] and, at this moment, we can not make any firm statement about distinctive nanocontact structure associated with this two limiting cases.

CONCLUSION AND FUTURE WORK

The research program MM 1593 has succeeded to demonstrate the functional magnetic field sensor devices based on nanocontact material with phase separated Ni and oxide/hydroxide domains ($Fe(OH)_3$). The observed values of ΔR/R are comparable if not better than today's state of the art GMR and TGMR based magnetic field sensors. The simplicity and cost effectiveness of the fabrication concept used for the prototype devices have a promising application for the development of the future magnetic field sensors based on ferromagnetic nanocontacts. In our work, the main result is that presence of electrochemically incorporated $Fe(OH)_3$ phase in Ni nanocontact matrix increases magnetoresistance values of the devices by factor of 10 to 50 as compared to the Ni single crystal nanocontact devices. This opens the frontier for future research on the materials that can be used for magnetic field sensors based on ferromagnetic nanocontacts. The relatively low values of R measured for the prototype devices with large ΔR/R indicate that electron conduction through the Ni phase is the main current path associated with measured resistance, however, positive and negative values of ΔR/R, as well as appearance of the hysterisis in magnetoresistance curves are indication that besides electron scattering from MDW some other more complex phenomena are contributing to the overall ΔR/R values. The future work on this interesting concept should be focused on several directions briefly described as:

1. Improvement of the fabrication methods in order to reach reduction of the nanocontact diameters below 10 nm, and thus provide the conditions for possible room temperature ballistic electron transport in the conductive channels of the nanocontact.
2. Optimization of Ni/$Fe(OH)_3$ nanocontact material composition, vol% of hydroxide phase, and electrodeposition process so that the higher values of ΔR/R can be obtained, explored.

3. Focusing on TEM investigation of the nanocontact structure and size of the $Fe(OH)_3$ phase in the Ni nanocontact body, and use this realistic dimensions to estimate the real cross-section of Ni conducting channels and use them as the input parameters in the physical models of the sensor device and for micromagnetic modeling.
4. Perform the device testing and magnetoresistance measurements at low temperatures as four probe and two probe resistivity measurements in order to get better distinction about the electron transport in the nanocontact devices (tunneling vs. ballistic contacts). Perform low temperature and room temperature I-V curves to get interpretation to what degree defects in the nanocontacts contribute to the measured value of the resistivity [46]. Low temperature I-V measurements and resistance measurements should also serve to estimate the relative ratio between physical dimensions of the nanocontact and the electron mean free path.

REFERENCES

1. S.R. Brankovic, S. –E. Bae, D. Litvinov, *Electrochemica Acta*, **53**, 5934 (2008).
2. J. George, S.-E. Bae, J. Rantschler, D. Litvinov and S. R. Brankovic, *J. Electrochem. Soc*, 155, D589 (2008).
3 . V. A. Parekh, A. Ruiz, P Ruchhoeft, S. R. Brankovic, and Dmitri Litvinov, *Nano Letters*. **7**, 3246 (2007).
4. N. Garcia, M. Muňoz, Y. -W. Zhao, *Phys. Rev. Lett*., **82**, 2923 (1999).
5. G. Tatara, Y. -W. Zhao, M. Muňoz, N. Garcia, Physical Review Letters, 83, 2030 (1999).
6. J.J. Verluijs, A. M. Bari, J. M. D. Coey, *Phys. Rev. Lett*, **87**, 026601 (2001)
7. S.H. Chung, M. Muňoz, N. Garcia, W.F. Egelhoff, R.D. Gomez, *Phys. Rev. Lett.*, **89**, 287203 (2002).
8. H.D. Chopra, and S.Z. Hua, *Phys. Rev.* **B**, 66, 020403 (2002)
9. M. Viert, S. Berger, M. Gaburaec, F. Ott, D. Olligs, I. Petej, J. F. Gregg, C. Fermon, G. Francinet, and G. LeGoff, *Phys. Rev.* **B, 66**, 220401 (2002).
10. S. Khizroev, Y. Hijazi, R. Chomoko, S. Mujherjee, R. Chantrell, X. Wu, R. Carley, D. Litvinov, *App. Phys. Lett.*, **86**, 042502 (2005)
11. G. A. Prinz, *Science*, **283**, 5400 (1999).
12. G.G. Cabrera and L.M. Falicov, *Phys. Stat. Sol.* **B**, **61**, 539 (1974)
13. H. Bruno, *Phys. Rev. Lett.*, **83**, 2425 (1999).

14. W.F. Egelhoff, L.Gan, H. Ettedgui, Y. Kadmon, C. J. Powell, P.J. Shapiro, R. D. McMichael, J. J. Mallett, T. P. Moffat, M.D. Stiles, and E. B. Svedberg, *J. of App. Phys.*, 95, 7554 (2004).
15. E. Y. Tsymbal, A. Sokolov, I.F. Sabirianov, and B. Doudin, *Phys. Rev. Lett.* **90,** 186602 (2003).
16. N. Garcia, *App. Phys. Lett.*, **77**, 1351 (2000).
17. J.D. Burton, A. Kashyap, M. Ye. Zhuravlev, R. Skomski, E. Tsymbal, S.S. Jaswal, O.N. Mryasov, and R. W. Chantrell, *Appl. Phys. Lett.*, **85**, 251 (2004).
18. N. Garcia, M. Muňoz, G.G. Qian, H. Roher, I. G. Savliev and Y. -W. Zhao, *Appl. Phys. Lett.*, **79**, 4550 (2001).
19. E. B. Svedberg, J.J. Mallet, H. Ettedgui, L. Gan, P.J. Chen, A.J. Shapiro, T. P. Moffat, and W. F. Egelhoff, *App. Phys. Lett.*, **84**, 236 (2004).
20. A. R. Despic in: *Comprehensive Treatise of Electrochemistry*, B. E. Conway, J. O'M. Bockris, E. Yeager, S. U. M. Khan, R. E. White, Editors, **vol. 7**, p. 451, Plenum Press, NY (1983).
21. N. Garcia, H. Cheng, H. Wang, N.D. Nikolic, C.A. Guerrero, A.C. Papageorgopoulos, *J. of Magn. Magn. Mater.* **272 -276**, 1722 (2004).
22. *Electrochemical Methods-Fundamentals and Application,* A.J. Bard, and L. R. Faulkner, Jonh Willey & Sons Inc., 2nd edition, New York (2001), p. 87, p. 632
23. M. Pourbaix, *Atlas of Electrochemical Equilibria in Aqueous Solutions,* NACE International, Houston (1974).
24. J.J. Mallett, E.B. Svedberg, H. Ettedgui, T. P. Moffat, and W.F. Egelhoff, *Phys. Rev.* **B, 70** 172406 (2004).
25. N. Garcia, H. Roher, I. G. Savliev and Y. -W. Zhao, *Phys. Rev. Lett.*, **85**, 3053 (2000).
26. X.M. Yang, A. Eckert, K. Mountfield, H. Gentile, C. Seiler, S. R. Brankovic, E.C. Johns, *J. Vac. Sci.Technol.* **B**, 21. 3017, (2003).
27. S. Gadad, and T. M. Harris, J. Electrochem. Soc. **145**, (1998) 3699.
28. I. Tabakovic, S. Remer, V. Inturi, P. Jalen, and A. Thayer, J. Electrochem. Soc., **147**, (2000) 219
29. T. Osaka, T. Yokoshima, D. Shinga, K. Imai, and K. Takashima., Electrochem. Solid State Lett., **6**, (2003) C53.
30 . B. D. Cullity, Introduction to Magnetic Materials, Addison-Wesley Pub. Comp. London, UK (1972) p.24 and p.152
31 . G. Barral, F. Njanjo-Eyoke and S. Maximovitch, *Electrochim. Acta,* **40,** 709 (1995)
32 . D. D. Macdonald, K. M. Ismail, E. Sikora, *J. Electrochem. Soc.*, **146**, 3142 (1998).
33 . V. Maurice, H. Talah, and P. Marcus, *Surface Science*, **304,** 98 (1994).
34. R. Nishimura, *Corrosion* **43**, 486 (1987)

35 .C. Sunseri, S. Piazza, F. Di Quarto, *Mater. Sci. Forum.* **185-188,** 435 (1995).
36 . W. Sugimoto et al, J. Phys. Chem. B, 109, 7330 (2006).
37 . S. R. Brankovic, K. Sendur, T. J. Klemmer, X. Yang, and E. C. Johns, in *Magnetic materials, processes, and devices VII and electrodeposition of alloys*, S. Krongelb, L. T. Romankiw, J.-W. Chang, Y. Kitamoto, J. W. Judy, C. Bonhote, G. Zangari and W. Schwarzacher Eds, PV2002-27, The Electrochemical Society INC, Pennington N. J. 2003. p. 269.
38 . S.R. Brankovic, X.M. Yang, T. Klemmer, and M. Seigler, *IEEE Trans. Magn.*, **42**, 132 (2006).
39. S. R. Brankovic, N. Vasiljevic, T. Klemmer and E.C. Johns, *J. Electrochem. Soc.* **152**, C196 (2005).
40 . J. A. Venables, G. D. Spiller and M. Hanbücken, *Rep. Prog. Phys.* **47**, 399 (1984).
41 . S. Stoyanov, I. Markov, *Surf. Sci.* **116**, 313 (1982).
42 . J. Tersoff, A.W. Denier van der Gon, and R.M. Tromp, *Phys. Rev. Lett.* **72,** 266 (1994).
43. L.-H. Tang, *J. Phys. I* (France) **3**, 935 (1993).
44 . R. C. Salvarezza and A.J. Arvia, in Electrochemical Nanotechnology, ed. W. J. Lorenz and W. Plieth, Wiley-VCH, New York (1998).
45. G. Wulff, *Z. Kristalogr.* **34**, 449 (1901).
46. *Introduction to Solid State Physics,* C. Kittel, John Willey & Sons, 8th Ed, New Jersey (2005), p. 148